Active elastic metamaterials for subwavelength wave propagation control

Y. Y. Chen & G. L. Huang

Acta Mechanica Sinica

ISSN 0567-7718

Acta Mech Sin
DOI 10.1007/s10409-015-0402-0

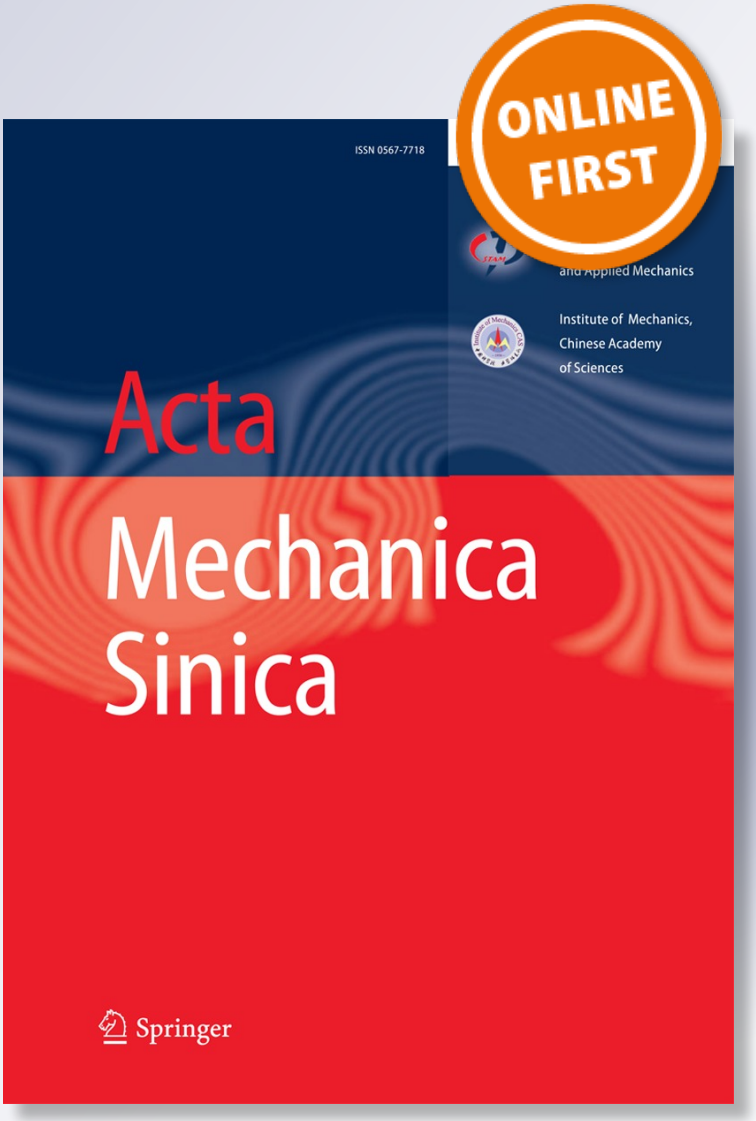

Springer

Acta Mech Sin
DOI 10.1007/s10409-015-0402-0

RESEARCH PAPER

Active elastic metamaterials for subwavelength wave propagation control

Y. Y. Chen[1] · **G. L. Huang**[1]

Received: 28 October 2014 / Revised: 13 November 2014 / Accepted: 12 January 2015

Abstract Recent research activities in elastic metamaterials demonstrate a significant potential for subwavelength wave propagation control owing to their interior locally resonant mechanism. The growing technological developments in electro/magnetomechanical couplings of smart materials have introduced a controlling degree of freedom for passive elastic metamaterials. Active elastic metamaterials could allow for a fine control of material physical behavior and thereby induce new functional properties that cannot be produced by passive approaches. In this paper, two types of active elastic metamaterials with shunted piezoelectric materials and electrorheological elastomers are proposed. Theoretical analyses and numerical validations of the active elastic metamaterials with detailed microstructures are presented for designing adaptive applications in band gap structures and extraordinary waveguides. The active elastic metamaterial could provide a new design methodology for adaptive wave filters, high signal-to-noise sensors, and structural health monitoring applications.

Keywords Active elastic metamaterials · Subwavelength wave control · Adaptive metastructures · Smart materials

1 Introduction

Continual research into advanced design techniques in electromagnetics, acoustics, and elasticity, such as the coordinate transformation method, triggered the development of multifunctional engineered composite materials, called metamaterials [1–12]. The focus of metamaterials is on the extreme range of characteristic material parameters, including negative values, high anisotropy, and exceeding gradient, owing to their specific microstructure design. The realization of acoustic/elastic metamaterials (EMMs) made it possible to achieve low-frequency sound/vibration attenuation, negative refraction, and acoustic/elastic lenses to control sound/elastic waves. Therefore, metamaterials extended significantly the spectrum for material selection and laid a new foundation for subwavelength wave propagation control. However, passive EMMs have limitations in real-time wave propagation control, which are mainly caused by frequency-dependent effective material parameters resulted from the locally resonant mechanism. The band gap from the current EMM design is fixed and limited to a narrow frequency band. Real-time geometrical adjustments of the resonator system are extremely difficult and unacceptable in practical applications. The ongoing technological material revolution in electro/magnetomechanical coupling provides a new choice in the development of active metamaterials. The full integration of adaptive materials, electronics, computing resources, and power systems with passive metamaterials can form a hybrid active metamaterial system whose material properties can be digitally and remotely controlled.

In recent years, much attention has been paid to piezoelectric materials in active or passive vibration control applications. As a promising passive technology, piezoelectric shunts have been widely adopted for mitigating structure flexible vibrations and absorbing sound energies [13–22]. In the passive shunt design, only external circuit elements are directly connected to the electrodes of the piezoelectric patch, where the energy generated by the piezoelectric patch

✉ G. L. Huang
huangg@missouri.edu

[1] Department of Mechanical and Aerospace Engineering, University of Missouri, Columbia, MO 65211, USA

Published online: 26 May 2015

induced by the host structure is consumed within an external circuit. With the shutting approach, the incident signal can be sensed simultaneously by the piezoelectric material, and the use of a passive network guarantees the stability of the coupled system. Forward first proposed the concept of a resonant circuit shunt to a piezoelectric actuator to reduce the vibration of a specific mode of an optical system [13]. According to the analysis of the equivalent circuit diagram, a resonant shunt can cancel the capacitive reactance of a piezoelectric element, and the circuit finally becomes pure resistive at the circuit resonant frequency to increase the attenuation of the mechanical system. By introducing electric degrees of freedom to systems with an external circuit, an analytical formulation of passive shunt networks was first developed by Hagood and Flotow [14]. A vibration absorber through single resistive–inductive (RL) shunting tuned at the resonance frequency of the circuit has been theoretically and experimentally demonstrated. To improve the attenuation ability of the shunting structure at a multimode or broadband frequency range, more complex shunting circuits have been investigated: multimode techniques [15,16], state switching [17], synthetic impedance [18], and negative impedance circuits [19–22]. Specifically, it has been experimentally demonstrated that the elasticity of piezoelectric materials shunted with negative capacitance circuits can be electrically tuned independently of frequency [23,24]. Based on this favorable property, periodic arrays of negative capacitance shunted piezoelectric patches were demonstrated numerically by employing a transfer matrix method to control the band gaps of a phononic beam [25]. By observing the link between shunted piezoelectric materials and periodically engineered phononic crystals and EMMs, several successful designs have been demonstrated for plate flexural wave attenuation using locally resonant shunts [26–29]. Both numerical and experimental results have shown that waves can be efficiently damped near the circuit resonant frequency and the tunability of wave band gap frequencies can be virtualized by circuit impedance adjustment. It is believed that the shunted piezoelectric material is a promising candidate in the design of active EMMs.

The magnetorheological/electrorheological (MR/ER) elastomer is another kind of prospective smart material in vibration and sound attenuation applications, with the shear modulus being controlled rapidly, continuously, and reversibly by applying an external magnetic/electric field [30–32]. An MR/ER elastomer usually functions by dispersing tiny ferrous/high electrical permittivity particles into an elastomer, such as synthetic and natural rubbers. The interaction of the chainlike structures formed within the elastomer can induce stiffening or softening of its modulus by an external magnetic/electric field. Recently, an MR/ER elastomer that overcomes sealing and environmental contamination problems in MR/ER fluid applications has attracted particular attention in the areas of tuned vibration absorbers and isolators. Based on a simple mass-spring system, Liao et al. [33] developed an ON–OFF control algorithm and designed a tunable isolator with a MR elastomer. The experimental results showed that the responses of the payload were suppressed significantly in comparison with a passive system. By discovering the relation between the phase advance of relative acceleration and the natural frequency of the primary system, a stiffness tuning algorithm is proposed for MR elastomer dynamic vibration absorbers [34]. Numerical simulations and experimental results demonstrate that the designed MR elastomer vibration absorber is highly adaptive in real-time control and the excitation frequency can be rapidly tracked. In elastic wave control applications, MR elastomers were integrated into a multilayer, one-dimensional phononic crystal to actively tune wave band gaps [35]. Due to the similarity of ER and MR elastomers, several vibration and wave control applications have also been found with ER elastomers [36–38]. For instance, a tunable band structure of locally resonant phononic crystals was investigated by applying various electric fields to ER elastomers embedded in an elastic matrix [38]. MR/ER elastomers would be another kind of attractive material in active EMM applications.

In this paper, we numerically demonstrate two types of active EMMs for subwavelength wave propagation control. In the first part, an active mass-in-mass lattice system with a negative capacitance piezoelectric shunting is studied to show the flexible band gap control. This promising application is then demonstrated with an active EMM plate for bending waves. The second part deals with the design and physical realization of a flexural waveguide and a focal lens based on active EMMs made with ER elastomers. A numerical simulation is conducted to demonstrate the tunability and flexibility of the proposed waveguide and lens over a broad frequency range, various steering directions, and different focal point locations without altering the microstructures.

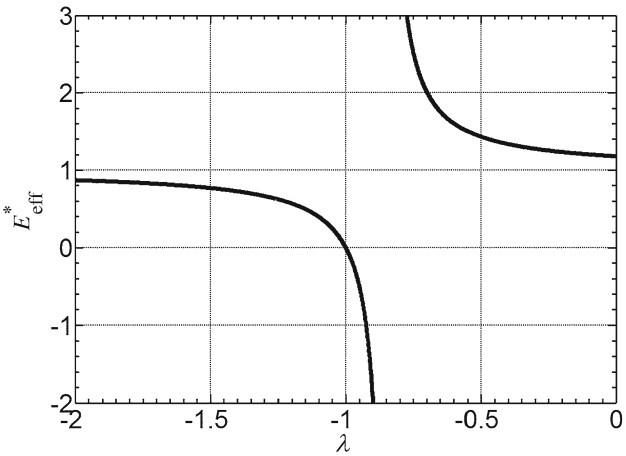

Fig. 1 Normalized effective modulus of piezoelectric patch with different NCRs

2 Band gap control in active EMMs with shunted piezoelectric patches

A frequency regime around the resonance frequency, also called a band gap, was observed in the EMM, in which the wave cannot propagate through and is trapped in the resonators. In this part, the wave band gap will be demonstrated to be tuned by a negative capacitance piezoelectric shunting in EMMs.

2.1 Negative capacitance piezoelectric shunting

Now consider a thin, shunted piezoelectric patch connected to a parallel negative capacitance $-C_n$. It is readily found that the shunted system is equivalent to a "simple" transducer with a lower capacitance. According to Hagood and Flotow, a modified effective Young's modulus of the shunted patch can be expressed according to the following expression, which is independent of frequency ω [14,39]:

$$E_p^{SU} = E_p^E \frac{C_p^T - C_n}{C_p^T\left(1 - k_{31}^2\right) - C_n}, \tag{1}$$

where $k_{31} = d_{31}/\sqrt{s_{11}\varepsilon_{33}}$ denotes the electromechanical coupling coefficient, with ε_{33}, d_{31}, and s_{11} being the dielectric constant, piezoelectric constant, and compliance of the piezoelectric patch, respectively, E_p^E is the Young's modulus of the piezoelectric material when the shunting network is in a short circuit configuration, and C_p^T is the electrical capacitance of the piezoelectric material at constant stress. The relationship between the open circuit Young's modulus and short circuit Young's modulus is [14,39]:

$$E_p^E = E_p^D\left(1 - k_{31}^2\right). \tag{2}$$

A significant result from Eq. (1) is that the shunt has the ability to modify elastic properties and, thus, may be used to control the dynamic behavior of the piezoelectric material.

Figure 1 shows the normalized effective modulus $E_{eff}^* = E_p^{SU}/E_p^D$ of PZT-5H as a function of the negative capacitance ratio (NCR), which is defined as $\lambda = -\frac{C_n}{C_p}$. It can be found that the normalized effective stiffness modulus is equal to the short circuit stiffness for large values of λ and equal to the open circuit stiffness for small values of λ. When λ approaches $-(1 - k_{31}^2)$ from small positive values, the effective modulus approaches positive infinity. However, when λ approaches $-(1 - k_{31}^2)$ from large positive values, the effective modulus is changed from a positive value to a negative value and eventually approaches negative infinity. The tunable modulus behavior of the shunted piezoelectric element will be used for the concept design of the active EMM.

2.2 Active mass-in-mass system

In this section, we will consider a one-dimensional lattice consisting of active mass-in-mass units, as shown in Fig. 2. The unit cells are placed periodically at a spacing of L. The two rigid masses are denoted by m_1 and m_2. The two spring constants k_1 and k_2 represent the interactions among the masses. Note that, in each unit cell, the inner spring constant with the negative capacitance piezoelectric shunting is denoted by $k_2(\lambda) = \frac{E_p^{SU} A_p}{l_p}$, which is a function of the NCR λ, where A_p and l_p are the cross-sectional area and length of the piezoelectric patch, respectively. Combining this with Eq. (1), the relationship of the stiffness and the shunted capacitance of the piezoelectric transducer can be established.

The variation in the band gap corresponding to different NCRs is shown in the shaded regions in Fig. 3. In the example, $m_2/m_1 = 9$, $k_1 = 10^8$ N/m, and the inner effective spring k_2 is calculated from the longitudinal deformation in the shunted piezoelectric (PZT-5H) beam. The material properties and dimensions of the piezoelectric patch are $\varepsilon_{33} = 3.10 \times 10^{-8}$ F/m, $d_{31} = -2.74 \times 10^{-10}$ C/m^2, $E_p = 60.6$ GPa, $A_p/l_p = 74.6 \times 10^{-6}$ m. In that case, the effec-

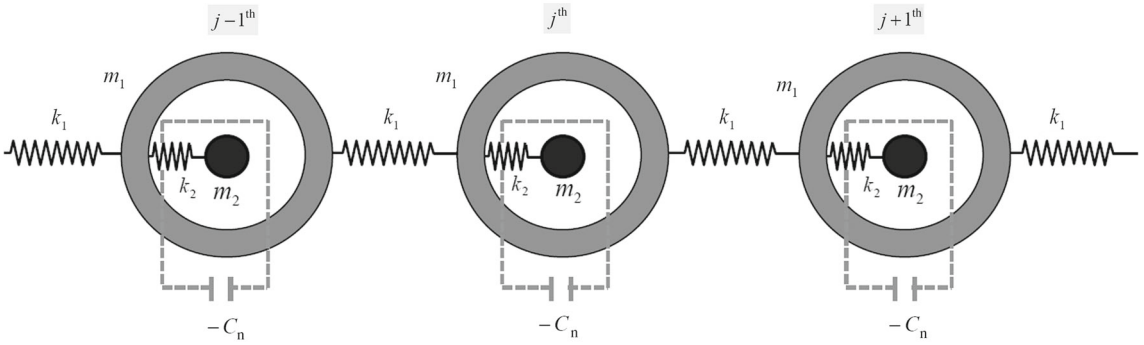

Fig. 2 Active mass-in-mass lattice system with inner spring to represent negative capacitance piezoelectric shunting

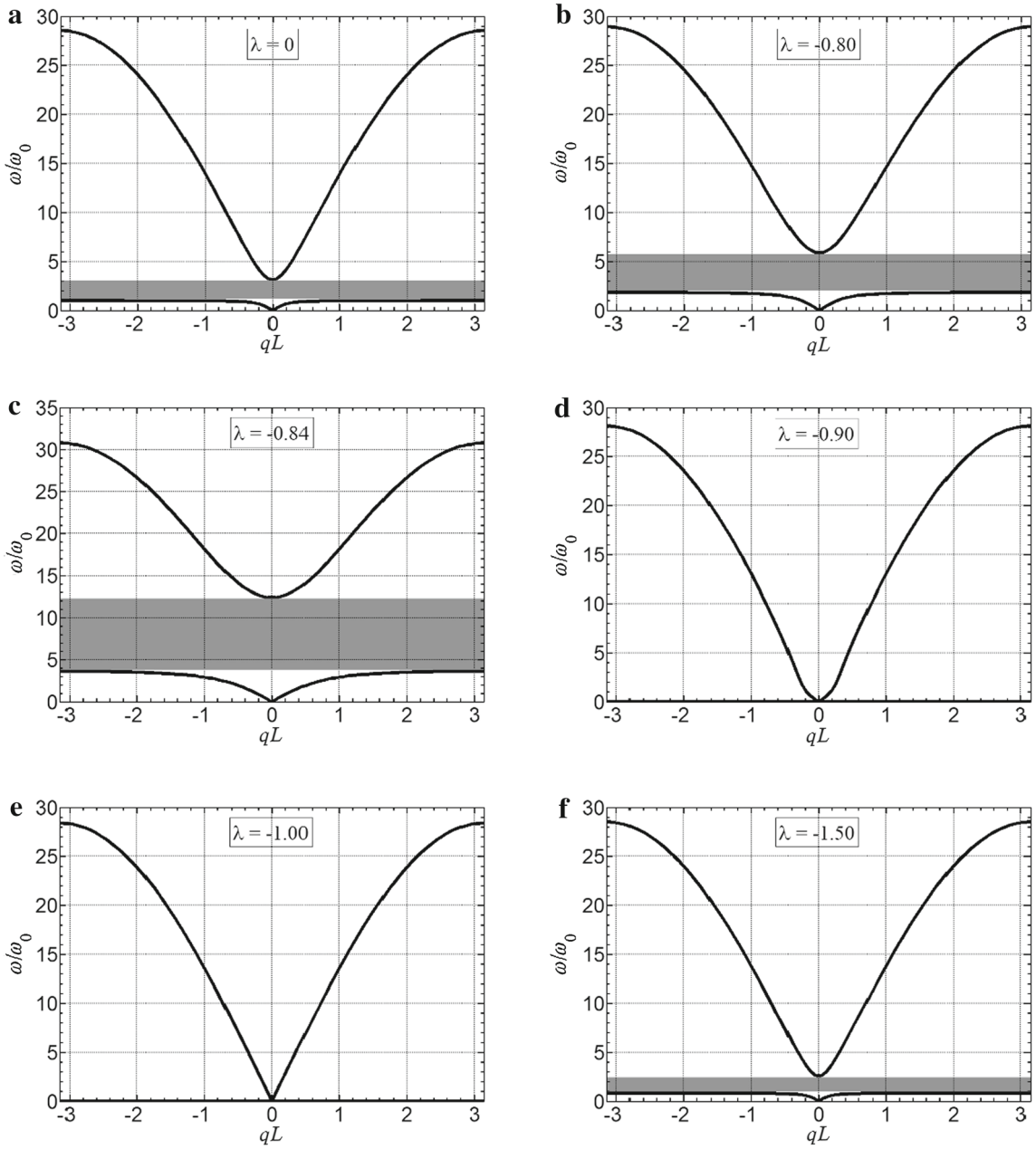

Fig. 3 Band gap of active mass-in-mass lattice system with different NCRs: **a** $\lambda = 0$. **b** $\lambda = -0.80$. **c** $\lambda = -0.84$. **d** $\lambda = -0.90$. **e** $\lambda = -1.00$. **f** $\lambda = -1.50$

tive stiffness of the piezoelectric material with an open circuit is represented by $k_2(\lambda = 0) = 4.46 \times 10^6$ N/m, with $k_2(0)/k_1 = 0.0446$. In the figures, $\omega_0 = \sqrt{k_2(0)/m_2}$ is the local resonance frequency of the resonator system with the open circuit. Figure 3a shows the band gap when $\lambda = 0$. The band gap is in the range of $\omega = \omega_0$–$3.2\omega_0$. The effective modulus of the shunted PZT patch will change with changes in the value of the connected negative capacitances, which induces band gap changes in the EMM. Figure 3b shows the band gap of the EMM when $\lambda = -0.8$ and the spring stiffness ratio $k_2(-0.8)/k_1$ increases. A comparison of the two diagrams shows that the width of the band gap has become slightly enlarged, and the band gap range has shifted from the original (ω_0–$3.2\omega_0$) to ($1.8\omega_0$–$5.9\omega_0$), as shown in Fig. 3b. Figure 3c shows the band gap of the EMM when $\lambda = -0.84$ and the spring stiffness ratio has become significantly larger. The width of the new band gap is significantly enlarged from the original (ω_0–$3.2\omega_0$) to ($3.6\omega_0$–$12.4\omega_0$). Therefore, the broadband frequency of the stop band could be tuned to (ω_0–$12.4\omega_0$) by connecting the active EMM to different negative capacitances. Figure 3d, e show the band structure diagrams of

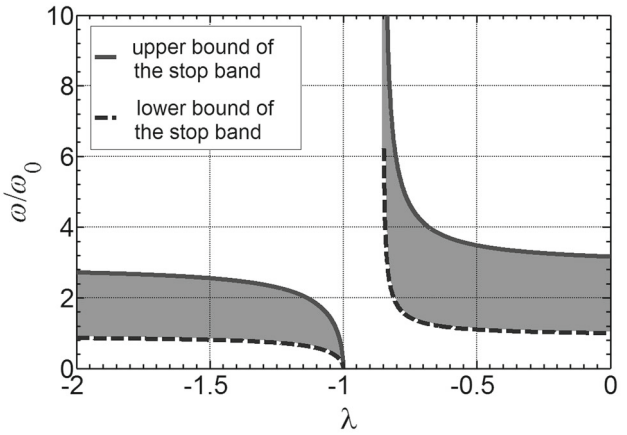

Fig. 4 Band gap variations of active mass-in-mass lattice system with different NCRs

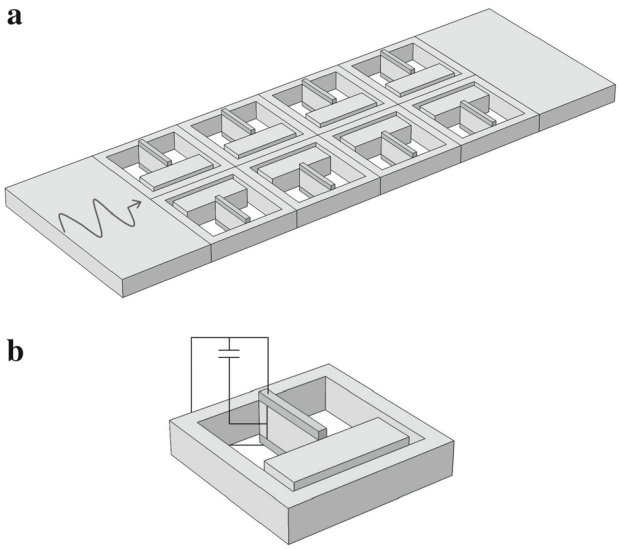

Fig. 5 **a** Active elastic metamaterial plate with a periodic array of a cantilever-mass system bonded by shunted piezoelectric patches. **b** Detailed microstructure in unit cell

the active EMM when $\lambda = -0.9$ and $\lambda = -1.0$, for which the spring stiffness ratio becomes negative and zero, respectively. In these two cases, the local resonance mechanism in the EMM is totally absent. The EMM now functions as the conventional material and the low-frequency stop band disappears. Figure 3f shows the band structure diagram of the EMM when $\lambda = -1.5$, in which the spring stiffness ratio becomes positive again with $k_2(-1.5)/k_1 = 0.006$. It is expected that the lower frequency band gap could be achieved in a range of $(0.8\omega_0$–$2.6\omega_0)$. If the NCR decreases further from $\lambda = -1.5$, the band gap will not change significantly.

Finally, the general variations in the band gaps of the EMM are shown in the shaded region in Fig. 4. In the figure, the solid red line represents the upper bound of the stop band, and the dashed blue line is the lower bound of the stop band. When the shunted piezoelectric NRC λ approaches -1.0 from negative infinity, the width of the band gap of the EMM will gradually decrease from the range $(\omega_0$–$2.8\omega_0)$ to zero. When λ is tuned from -1.0 to $-(1 - k_{31}^2)$, the EMM will become a conventional material and the stop band will disappear. Similarly, when the value of λ is changed from $-(1 - k_{31}^2)$ to 0 (open circuit), one can find that the bandwidth of the stop band of the EMM will be greatly reduced from a large bandwidth to a normal EMM band gap range of $(\omega_0$–$3.2\omega_0)$. The result of the active EMM provides a very promising solution in overcoming the fixed band gap in the EMM, and the location and width of the band gaps are actively tunable.

2.3 Band gap control in an active EMM plate

A thin EMM plate with periodic cantilever-mass microstructures was proposed for low-frequency band gap applications [11]. In this section, we illustrate the practical application of how the periodic array of shunting piezoelectric patches bonded to a cantilever beam can function as the building block of an active EMM.

Figure 5a shows an active EMM plate with a periodic array of cantilever masses bonded by shunted piezoelectric patches. The detailed microstructure in the unit cell is shown in Fig. 5b. The plate behaves as a one-dimensional waveguide that supports the propagation of transverse waves. In the low-frequency range, the behaviors of micro beams of resonators can be conveniently described through the Euler–Bernoulli theory with piecewise elastic and mass properties. The negative capacitance shunts are applied to piezoelectric patches installed in a periodic array, which consists of a series of equally spaced piezoelectric patches.

The thin plate beam is made of stainless steel ($E_s = 195$ GPa, $\rho_s = 8000$ kg /m^3, $\upsilon_s = 0.33$) with a thickness of $t_s = 1$ mm and width of $b_s = 0.45$ mm. The shunted piezoelectric materials are PZT-5H ($E_p = 60.6$ GPa, $\rho_p = 7500$ kg/m^3, $\upsilon_p = 0.34$) with a thickness of $t_p = 0.1$ mm, a length of $l_p = 2.7$ mm, and a width of $b_p = 0.45$ mm. The spacing of the adjacent unit cells is $a = 5.6$ mm.

Figure 6 shows the band gap variation (shaded regions) of the active EMM plate with surface-bonded piezoelectric patches with different NCRs $\lambda = -\frac{C_n}{C_p}$ for the out-of-plane bending wave. Figure 6a shows the band gaps when $\lambda = 0$, i.e., the shunting circuits are open. In the figures, ω_0 is the local resonance frequency of the cantilever resonator system with an open circuit. The first band gap is in the range of $\omega = \omega_0$–$1.5\omega_0$. Figure 6b shows the dispersion diagram and the first band gap of the EMM plate when $\lambda = -0.83$,

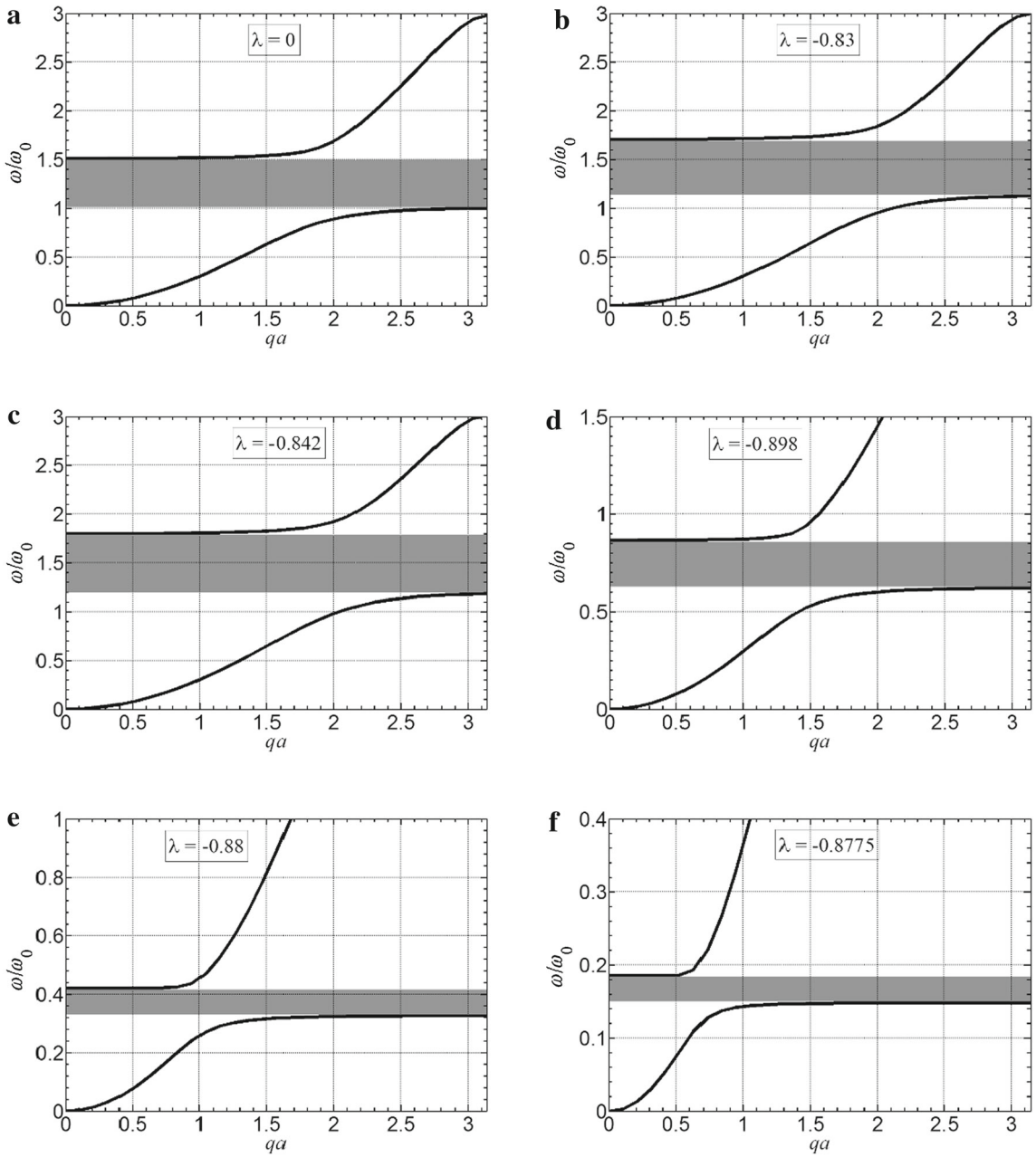

Fig. 6 Band gap variation of active elastic metamaterial plate with different NCRs for out-of-plane bending wave: **a** $\lambda = 0$. **b** $\lambda = -0.83$. **c** $\lambda = -0.842$. **d** $\lambda = -0.898$. **e** $\lambda = -0.88$. **f** $\lambda = -0.8775$

in which the effective modulus of the shunted piezoelectric patch increases in a positive value, and thus the bending stiffness of the cantilever beam is increased. The width of the band gap remains almost unchanged; however, the frequency range of the first band gap is shifted from the original (ω_0–$1.5\omega_0$) to ($1.13\omega_0$–$1.7\omega_0$). Figure 6c shows a dispersion diagram and the first band gap of the EMM plate when $\lambda = -0.842$, in which the value of the effective stiffness of the shunted piezoelectric patch continuously increases in a positive direction. The first band gap is shifted from the original band gap (ω_0–$1.5\omega_0$) to ($1.19\omega_0$–$1.8\omega_0$). However, if the effective stiffness of the shunted piezoelectric patch continuously increases to a larger value, the local resonance can be induced in the cantilever beam in the low-frequency range only with great difficulty because of the finite stiffness in the host medium. Figure 6d shows a band structure diagram of the EMM plate when $\lambda = -0.898$, in which the effective modulus of the shunted piezoelectric patch becomes a negative value, and therefore the effective bending stiffness of the cantilever beam decreases. Comparing the band diagram with the open circuit, it is found that the band gap is shifted from the original band gap (ω_0–$1.5\omega_0$) to

($0.62\omega_0$–$0.87\omega_0$). Figure 6e, f shows a band structure diagram of the EMM plate when $\lambda = -0.88$ and $\lambda = -0.8775$, respectively, in which the effective stiffness of the shunted piezoelectric patch is further reduced to a negative value. It is seen that the extremely low-frequency band gaps are located in ranges of ($0.33\omega_0$–$0.42\omega_0$) and ($0.15\omega_0$–$0.19\omega_0$) for both cases. However, the width of the stop band becomes very narrow in the low-frequency cases for the bending wave. One important requirement for achieving a tunable band gap is to have the ability to adjust the value of the negative capacitance very accurately.

2.4 Conclusions

In this part, we first investigate dispersion curves and band gap control in an active mass-in-mass lattice system. The unit cell of the lattice system consists of inner masses connected by active linear springs to represent negative capacitance piezoelectric shunting. It is demonstrated that the band gaps can be actively controlled and tuned by varying the effective spring constant by applying negative capacitance. Subsequently, this technique is implemented in an active EMM plate with periodically surface-bonded piezoelectric patches that are shunted with a negative capacitive circuit. It is demonstrated that the location and range of an induced band gap of an active EMM plate can be effectively tuned by using shunted piezoelectric patches with different NCRs, especially for extremely low-frequency cases.

3 Control of flexural waves in active EMMs with ER elastomers

Flexural waves in plates have been extensively employed in structural health monitoring owing to their capacity for long-range and through-the-thickness interrogation of structures [9,40,41]. To achieve high-resolution damage detection, controlling flexural wave propagation paths is essential in both emitting and receiving processes. For example, when a monitored object is not in the ray direction of a flexural wave propagation, a waveguide structure could steer the wave in a desired direction. On the other hand, flexural wave focusing can increase the signal-to-noise ratio of sensor signals, thereby improving the damage detection resolution [9]. Designing a waveguide device to achieve full control of flexural waves would be of great benefit to the development of structural health monitoring and new sensors. In this part, we numerically demonstrate the design and physical realization of a flexural waveguide and a focal lens based on an active EMM with ER elastomers.

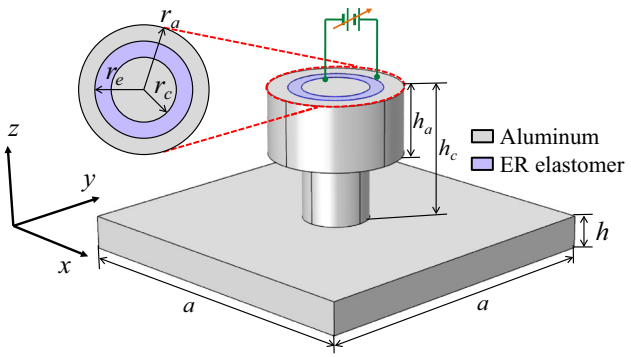

Fig. 7 Unit cell of active EMM surface-bonded on plate

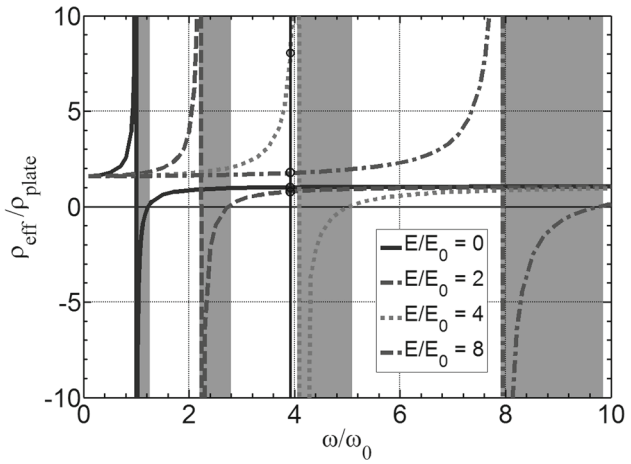

Fig. 8 Effective mass density of EMM under various magnitudes of electric fields

Table 1 Unit cell geometrical and material parameters of active EMM

Geometrical properties (mm)		Material properties	
a	5	Mass density (aluminum)	2700 kg/m^3
h	1.5	Lamé's first parameter (aluminum)	51 GPa
r_a	2	Shear modulus (aluminum)	26 GPa
r_e	0.7	Mass density (ER elastomer)	1000 kg/m^3
r_c	0.5	Lamé's first parameter (ER elastomer)	1532 KPa
h_a	2	G_0	64 KPa
h_c	1.8	E_0	1.3 kV/mm

3.1 ER elastomers

An ER elastomer is a kind of soft smart material with the shear modulus being controlled by application of an external magnetic/electric field [42]. Theoretically, the relation between the dynamic shear modulus of an ER elastomer, G, and the

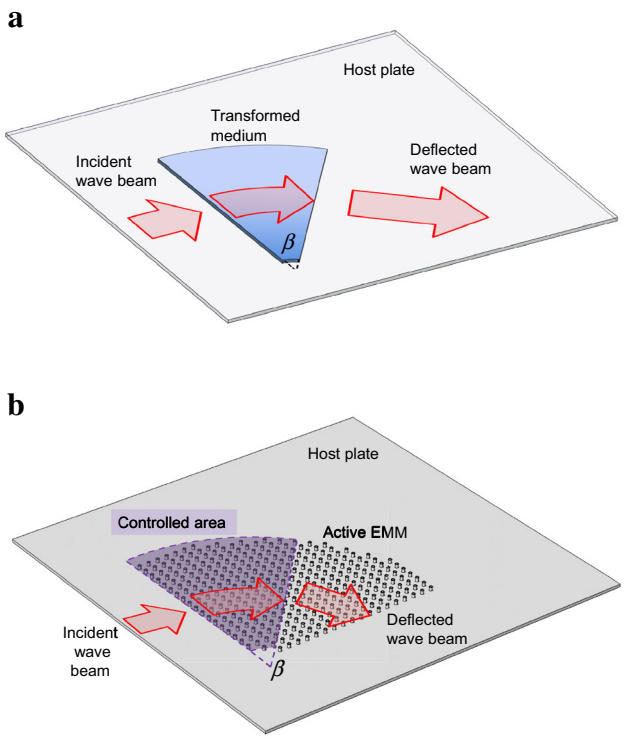

Fig. 9 **a** Schematic of a flexural waveguide with a deflection angle β using the transformation method. **b** Physical realization of flexural waveguide equipped with array of active EMMs

applied electric field of magnitude, $\bar{E}$, can be approximately expressed as [38,42]

$$G = G_0\left[1 + \left(\bar{E}/E_0\right)^2\right], \tag{3}$$

where G_0 is the shear modulus without an electric field, and E_0 is a reference electric field. Based on Eq. (3), it can be concluded that the electric field has the ability to modify elastic properties and, thus, may be used to control the dynamic behavior of the ER elastomer.

3.2 Active EMM for flexural waveguide and focal lens

The unit cell design of the considered active EMM with tunable material parameters over a broad frequency range is schematically shown in Fig. 7, where an active resonator is equipped with an ER elastomer annulus sandwiched between an aluminum annular ring and an aluminum cylinder. The resonator is surface-bonded on the top of the host plate. In the figure, a and h are the side length and the thickness of the unit lattice of the aluminum host plate, respectively. The radius and height of the aluminum cylinder are denoted respectively by r_c and h_c. The height and outer radiuses of the ER elastomer and aluminum annuluses are represented by h_a, r_e and r_a, respectively.

The working mechanism of the EMM can be briefly described as follows. When a bending wave propagates in the host plate with the surface-bonded EMM, the outer aluminum ring will vibrate up and down with respect to the plate, and the ER elastomer will undergo shear-mode deformation. In the presence of the out-of-phase motion of the outer aluminum ring with respect to the host plate, the flexural wave energy is trapped in the resonator and an omnidirectional wave band gap will be observed, which can be interpreted by the negative effective mass density of the system [5]. In addition, the tunability and flexibility of the active EMM can be accomplished by tuning the shear modulus of the ER elastomer annulus under electric fields adjusted in a timely manner along the radial direction without altering the microstructures.

The numerically based effective medium method is used to determine the out-of-plane effective mass density of the EMM [9]. Figure 8 shows the normalized effective mass densities of the proposed EMM under various magnitudes of applied electric fields using the finite-element software COMSOL Multiphysics. In the figure, ω_0 is the resonant frequency of the outer aluminum ring, with $\bar{E} = 0$, and the microstructure dimensions and material properties of the EMM are listed in Table 1.

As shown in the figure, the effective mass density reaches positive infinity at the resonant frequency and immediately turns to negative infinity, then gradually approaches a positive constant value at higher frequencies. Negative effective mass densities (shaded areas) can be found near the resonant frequency, i.e., $\omega = \omega_0$–$1.3\omega_0$, when $\bar{E} = 0$. It can also be observed that the frequency range of the negative effective mass density can be shifted by changing the magnitudes of the applied electric fields. For example, when $\bar{E} = 2E_0$, $4E_0$, and $8E_0$, the frequency range shifts to $2.2\omega_0$–$2.8\omega_0$, $3.9\omega_0$–$5.1\omega_0$, and $8.1\omega_0$–$9.8\omega_0$, respectively. This is understandable because the shear modulus of the ER elastomer increases as the magnitude of the electric field increases, according to Eq. (3), which will result in a shift in the resonant frequency. In addition, the frequency range of the negative effective mass density increases with increases in the magnitude of the electric field. Finally, an extreme gradient distribution of the effective mass density of the EMM can be accomplished by applying various magnitudes of electric fields at different frequencies. For example, as shown in the figure at $\omega = 3.9\omega_0$, the normalized effective mass density can be varied as 1.008, 0.7874, 7.555, and 1.758 when the electric field is tuned to $\bar{E} = 0, 2E_0, 4E_0$, and $8E_0$, respectively, which provides a potential solution for wave steering lens devices. It should be mentioned that the tunability of the effective mass density through electric fields could be implemented very fast and in real time, which opens up new possibilities for many practical applications of the active EMM.

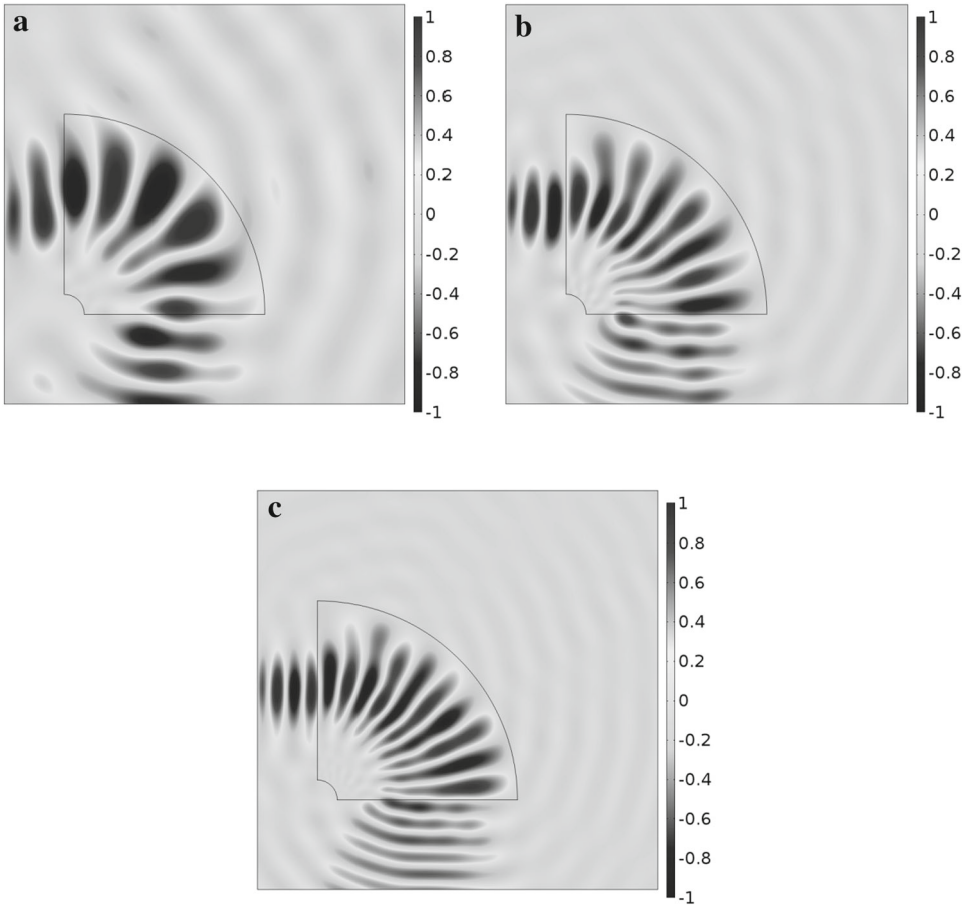

Fig. 10 Normalized out-of-plane wave field of a 90° flexural waveguide with material parameters from transformation method at different incident frequencies: **a** 15 kHz. **b** 30 kHz. **c** 50 kHz

3.3 Flexural waveguide with active EMMs

Up to this point, a flexural waveguide with a gradient material parameter profile can be readily made with an array of surface-bonded active EMMs. The tunability and flexibility of the waveguide will be discussed for the case of extraordinary wave steering over a broad frequency range.

Figure 9a shows a schematic model of the flexural waveguide with an arbitrary steering angle β using the coordinate transformation method. According to the relations between the material properties and principal stretches [43,44], there exist many options for material property selection of the transformed medium. For ease of physical realization, the relationship between the transformed medium and the host plate is selected as [43]

$$E' = E, \tag{4a}$$

$$\rho' = \left(\frac{R_0}{r'}\right)^4 \rho, \tag{4b}$$

where E' and ρ' are the Young's modulus and mass density of the transformed media, respectively, E and ρ are the Young's modulus and mass density of the host plate, respectively, r' is the transformed physical polar coordinate, and R_0 is a constant.

As illustrated in the figure, an incident flexural wave beam is launched toward the designed waveguide, and the wave is then steered along the waveguide with a beam deflection angle β. Figure 9b shows the physical realization of the waveguide using an array of the proposed active EMMs with a 90° circular sector. The mass density profile of the waveguide from the transformation method will be approximately truncated by the discretely distributed EMMs under various electric fields. Applied electric fields are numerically determined through wave dispersion analysis. For the array of EMMs with a 90° sector, as shown in Fig. 9b, the beam deflection angle β ($0° < \beta < 90°$) can be actively adjusted by properly selecting the controlled area of the EMMs.

Figure 10 shows the out-of-plane wave field of the flexural waveguide with a deflection angle of 90° based on the transformed material parameters [Eq. (4)] at frequencies of 15, 30, and 50 kHz. In the model, perfectly matched layers (PMLs) on the host plate are adopted to simulate infinite boundaries

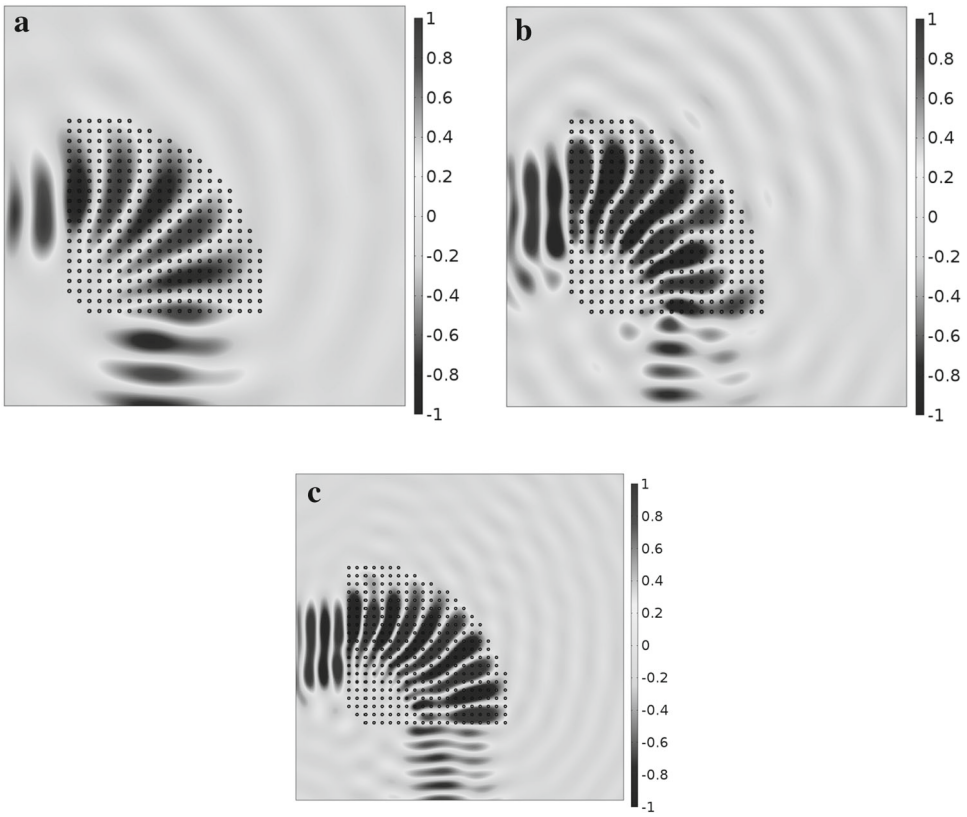

Fig. 11 Normalized out-of-plane wave field of 90° flexural waveguide equipped with array of active EMMs at different incident frequencies: **a** 15 kHz. **b** 30 kHz. **c** 50 kHz

for flexural wave propagation. The material parameters of the host plate are the same as those listed in Table 1. The waveguide is designed with inner and outer radii of the circular sector of 10 and 100 mm, respectively. A harmonic antisymmetric Gaussian displacement profile is launched along the left edge of the plate. It can be observed that the direction of the flexural waves can almost be deflected to 90° at different frequencies. Small reflections are found at the interfaces between the waveguide and the background plate owing to the material mismatch between the host medium and transformed medium. Scattered waves in the host plate leaking from the waveguide are also observed, which is caused by the width expansion of the Gaussian beam. Specifically, when the incident frequency increases from 15 to 50 kHz, the scattered wave becomes nearly invisible.

For the physical realization of the waveguide, an array of active EMMs is proposed. Figure 11 presents a numerical demonstration of the flexural waveguide using the active EMM at different operating frequencies of 15, 30, and 50 kHz. For the active EMM, the outer radius of the aluminum ring r_a is selected as 0.9 mm, and other geometrical and material parameters are the same as those used in Fig. 8. In the simulation, the required mass density profiles at different frequencies are approximated by the discretely distributed EMM by actively adjusting the applied electric field on the ER elastomer without altering the microstructure. It is found that the flexural waves are indeed steered to 90° as desired at all frequencies. Very good agreement with results predicted from the transformation method is observed, which shows the feasibility of the proposed active EMM. It is noticed that interior scattering waves within the discretely distributed EMM nearly vanish because of the unique subwavelength feature of the proposed EMM compared with the wavelength of the operating frequency in the host plate.

Figure 12 shows the out-of-plane wave field of the flexural waveguide based on the proposed EMM at an operating frequency of 15 kHz, with deflection angles of 15°, 45°, and 60°, respectively. In the simulation, the material and geometrical parameters of the active EMM are the same as those used in Fig. 11. As illustrated in the figure, the deflection angle can be flexibly tuned by applying electric fields on the selected areas (shaded areas) of the active EMM without altering the microstructures. The implied wave mechanism is that the effective mass density in the unselected area of the EMM is close to the mass density of the host plate at the operating frequency; therefore, effects on the flexural wave propagation due to the bonded EMM can be ignored.

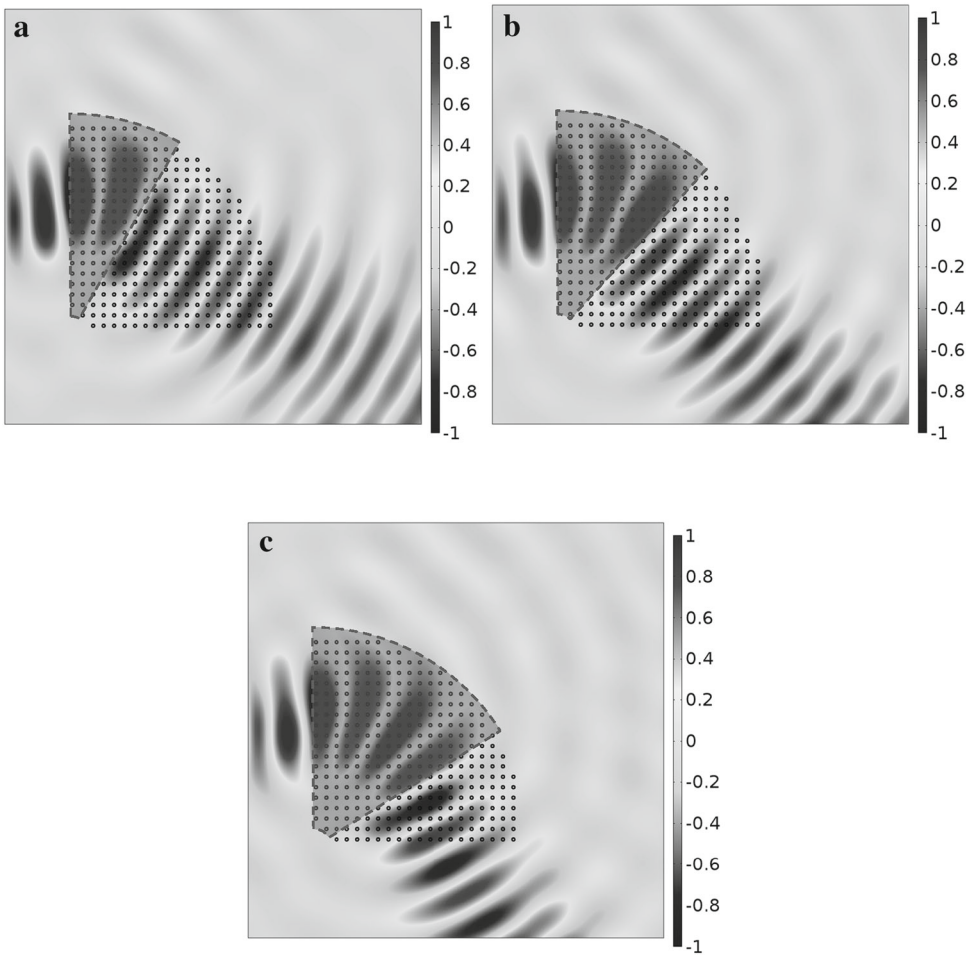

Fig. 12 Normalized out-of-plane wave field of flexural waveguide with controlled active EMMs at operating frequency of 15 kHz with various deflection angles: **a** 15°. **b** 45°. **c** 60°

3.4 Focal lens with active EMMs

The proposed surface-bonded active EMM in waveguide applications can also be implemented as a flexural wave focal lens. The tunability of the focal lens will be demonstrated with the location variation of the focal spot.

Figure 13a shows a schematic model of the focal lens in a host plate. The hyperbolic index profile, which has been widely employed in optical, acoustical, and elastic wave focusing applications [9,45,46], is expressed as

$$n(y) = n_0 \, \mathrm{sech}^2(\alpha y), \tag{5}$$

where y is a Cartesian coordinate in the neutral plane of the host plate and perpendicular to the incident wave propagation direction with its origin at the center of the focal lens, n_0 is the index at the origin, and α is the gradient constant for determining the location of the focal spot within the lens material. For ease of physical realization, the material parameters of the focal lens are selected as [46]

$$\hat{E} = E, \tag{6a}$$

$$\hat{\rho} = \rho \left[\mathrm{sech}^2 (\alpha y) \right]^4, \tag{6b}$$

where $\hat{E}$ and $\hat{\rho}$ are the Young's modulus and mass density of the lens material, respectively.

As illustrated in the figure, an incident flexural wave beam is launched toward the designed focal lens, and the wave is then focused in a small region. Figure 13b shows the physical realization of the focal lens using an array of the proposed active EMMs. The mass density profile of the focal lens from Eq. (6) will be approximately truncated by the discretely distributed EMMs under various electric fields. Applied electric fields are numerically determined through wave dispersion analysis.

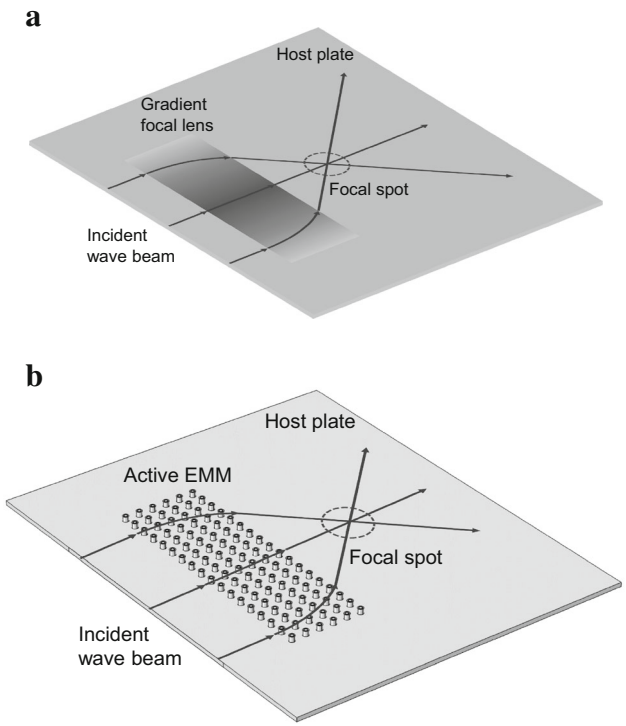

Fig. 13 **a** Schematic of hyperbolic focal lens in host plate. **b** Physical realization of focal lens equipped with array of active EMMs

Figure 14 shows the out-of-plane wave field of the flexural focal lens based on the proposed material profile (Fig. 14a, c) and the discrete EMM (Fig. 14b, d) at an operating frequency of 50 kHz, with α being 45 and 30 m^{-1}, respectively. In the simulation, the material and geometrical parameters of the active EMM are the same as those used in Figs. 11 and 12. Good agreement is observed. As illustrated in the figure, the location of the focal spot can be flexibly tuned by applying different electric fields to achieve various index profiles. The implied wave mechanism is that a wave cannot be focused on a single point owing to the different refraction coefficients on the right edge of the lens. It is also found that the focusing efficiency becomes weaker as α gets smaller. Modified focusing index profiles may be needed for elastic waves to improve the signal-to-noise ratio when the focusing location is far from the lens.

3.5 Conclusions

In this part, we have designed an active EMM and physically realized a flexural waveguide and a focal lens that can fully control the flexural wave propagation in a plate. The physical realization is suggested by using the active EMM in the form of discretization and truncation. The tunable effective mass density is accomplished by applying an adjustable electric field in an ER elastomer under shear mode deformation. Finally, a numerical simulation was conducted to demonstrate the tunability and flexibility of the proposed waveguide and lens over a broad frequency range, various steering directions, and different focal locations without altering the microstructures.

4 Control of longitudinal waves with shunted piezoelectric patches

Elastic wave propagation control using the tuned material effective mass density was discussed in previous sections. Since there is no unique transformation relation in elastodynamics, a beam bender can also be designed using a controlled modulus and constant density. Elastodynamic transformation relations for longitudinal waves have been derived by Chang et al. [44] as

$$\bar{E}' = \left(\frac{r'}{R_0}\right)^2 E, \tag{7a}$$

$$\bar{\rho}' = \rho, \tag{7b}$$

where $\bar{E}'$ and $\bar{\rho}'$ are the Young's modulus and mass density of the transformed medium, respectively. In the simulation, shunted piezoelectric patches are surface-bonded to the host plate as modulus controlling components. Figure 15 shows a schematic of the beam bender of a plate structure bonded by piezoelectric patches with shunted negative capacitance.

As illustrated in the figure, an array of shunted piezoelectric patches is bonded on an aluminum plate in a 90° circular sector. To match the effective Young's modulus profile given by the transformation relations [Eq. (7a)], the circular sector is discretized into several small sections, and each section is individually shunted with the corresponding negative capacitance. The applied negative capacitance is calculated based on the effective medium theory and Eq. (1). An incident longitudinal wave beam is launched toward the designed beam bender.

Figure 16 shows the divergence field of displacements of the beam bender with the deflection angle being 90° based on the transformed material parameters [Eq. (7a)] at a frequency of 150 kHz. In the model, PMLs on the host plate are adopted to simulate infinite boundaries for longitudinal wave propagation. The material parameters of the host plate and shunted piezoelectric material are the same as those listed in Table 1 and those for Fig. 6. The beam bender is designed with inner and outer radii of the circular sector of 60 and 150 mm and R_0 of 75 mm. A harmonic Gaussian displacement profile is launched along the left edge of the plate. It can be observed that the direction of the longitudinal wave can be deflected to 90° at

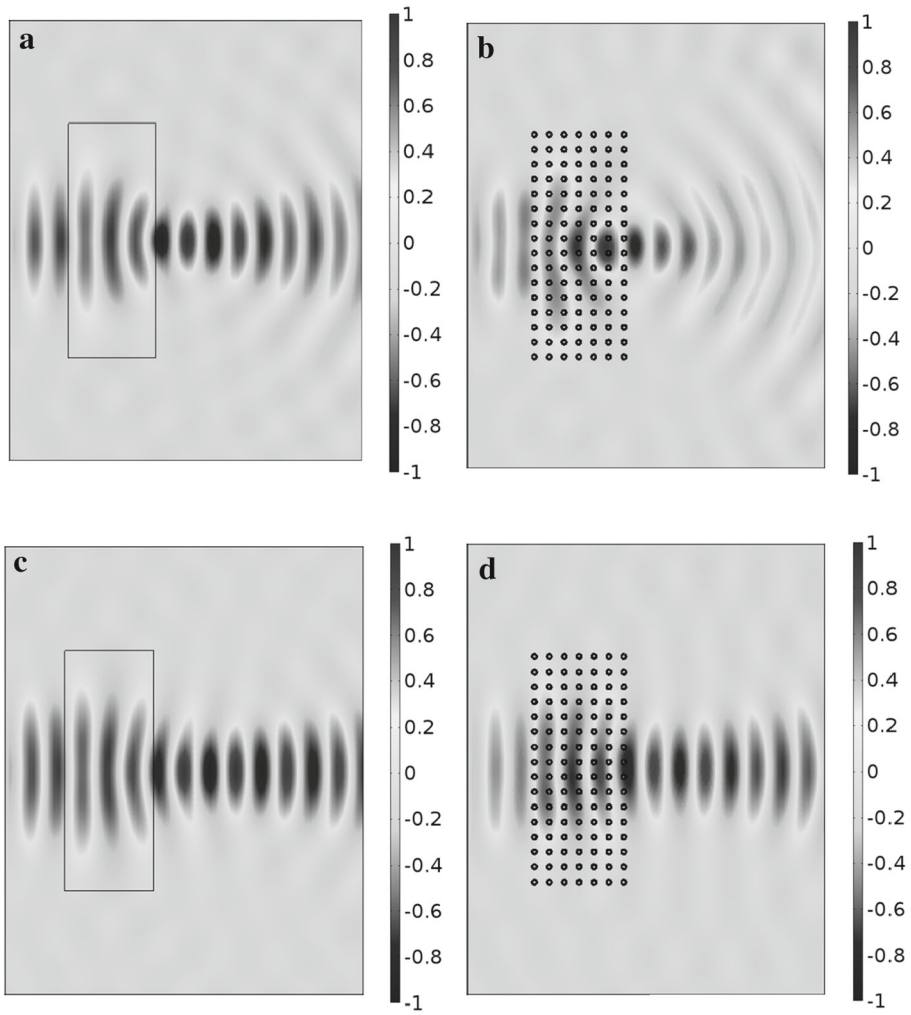

Fig. 14 Normalized out-of-plane wave field of focal lens with effective material parameters and controlled active EMMs at operating frequency of 50 kHz with various gradient constants: **a** Effective material parameters ($\alpha = 45\ \mathrm{m}^{-1}$). **b** Active EMMs ($\alpha = 45\ \mathrm{m}^{-1}$). **c** Effective material parameters ($\alpha = 30\ \mathrm{m}^{-1}$). **d** Active EMMs ($\alpha = 30\ \mathrm{m}^{-1}$)

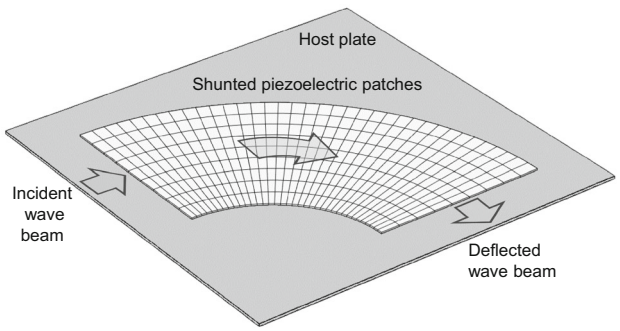

Fig. 15 Schematic of beam bender with shunted piezoelectric materials

this frequency. Small reflections are found at the interfaces between the beam bender and the background plate as a result of the material mismatch between the host medium and transformed medium. In addition, scattered waves in the host plate leaking from the waveguide are also observed, which is caused by the width expansion of the Gaussian beam.

5 Conclusions

In this paper, two types of active EMMs with shunted piezoelectric materials and ER elastomers are proposed. Theoretical analyses and numerical validations of the active EMMs with detailed microstructures are presented for designing adaptive applications in band gap structures and extraordinary waveguides by adjusting circuit element parameters and applied electric fields without altering the microstructures. This new concept and technology should lead to new rel-

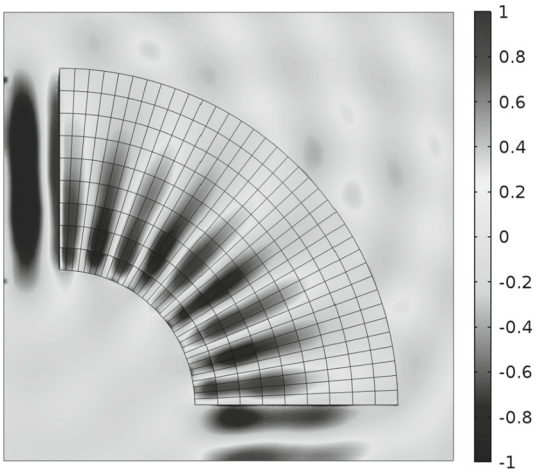

Fig. 16 Divergence field of displacements of a 90° beam bender bonded with an array of negative capacitance shunted piezoelectric patches at a frequency of 150 kHz

evant applications for noise or vibration control, integrated surface actuators, or microacousto-optic devices for adaptive applications in telecommunications and the health monitoring of structures.

Acknowledgments This work was supported by the Air Force Office of Scientific Research under Grant AF 9550-15-1-0061 with Program Manager Dr. Byung-Lip (Les) Lee.

References

1. Pendry, J.B., Holden, A.J., Robbins, D.J., et al.: Magnetism from conductors and enhanced nonlinear phenomena. IEEE Trans. Microw. Theory Tech. **47**, 2075–2084 (1999)
2. Smith, D.R., Padilla, W.J., Vier, D.C., et al.: Composite medium with simultaneously negative permeability and permittivity. Phys. Rev. Lett. **84**, 4184–4187 (2000)
3. Liu, Z., Zhang, X., Mao, Y., et al.: Locally resonant sonic materials. Science **289**, 1734–1736 (2000)
4. Fang, N., Xi, D., Xu, J., et al.: Ultrasonic metamaterials with negative modulus. Nat. Mater. **5**, 452–456 (2006)
5. Huang, H.H., Sun, C.T., Huang, G.L.: On the negative effective mass density in acoustic metamaterials. Int. J. Eng. Sci. **47**, 610–617 (2009)
6. Yang, Z., Mei, J., Yang, M., et al.: Membrane-type acoustic metamaterial with negative dynamic mass. Phys. Rev. Lett. **101**, 204301 (2008)
7. Mei, J., Ma, G., Yang, M., et al.: Dark acoustic metamaterials as super absorbers for low-frequency sound. Nat. Commun. **3**, 756 (2012)
8. Liu, X.N., Hu, G.K., Huang, G.L., et al.: An elastic metamaterial with simultaneously negative mass density and bulk modulus. Appl. Phys. Lett. **98**, 251907 (2011)
9. Yan, X., Zhu, R., Huang, G.L., et al.: Focusing guided waves using surface bonded elastic metamaterials. Appl. Phys. Lett. **103**, 121901 (2013)
10. Wu, Y., Lai, Y., Zhang, Z.Q.: Elastic metamaterials with simultaneously negative effective shear modulus and mass density. Phys. Rev. Lett. **107**, 105506 (2011)
11. Zhu, R., Huang, G.L., Huang, H.H., et al.: Experimental and numerical study of guided wave propagation in a thin metamaterial plate. Phys. Lett. A **357**, 2863–2867 (2011)
12. Zhu, R., Liu, X.N., Hu, G.K., et al.: An chiral elastic metamaterial beam for broadband vibration suppression. J. Sound Vib. **333**, 2759–2773 (2014)
13. Forward, R.L.: Electronic damping of vibrations in optical structures. J. Appl. Opt. **18**, 690–697 (1979)
14. Hagood, N.W., Flotow, A.V.: Damping of structural vibrations with piezoelectric materials and passive electrical networks. J. Sound Vib. **146**, 243–268 (1991)
15. Wu, S.Y.: Method for multiple-mode shunt damping of structural vibration using a single PZT transducer. In: Proceedings of SPIE smart structures and materials, smart structures and intelligent systems, Huntington Beach, CA (1998)
16. Wu, S.Y., Bicos, A.S.: Structural vibration damping experiments using improved piezoelectric shunts. In: Proceedings of SPIE smart structures and materials, San Diego, CA, 3–5 March, 40–50 (1997)
17. Corr, L.R., Clark, W.W.: Comparison of low-frequency piezoelectric switching shunt techniques for structural damping. Smart Mater. Struct. **11**, 370–376 (2002)
18. Fleming, A.J., Belirens, S., Moheimani, S.O.R.: Synthetic impedance for implementation of piezoelectric shunt damping circuits. Electron. Lett. **36**, 1525–1526 (2000)
19. Behrens, S., Fleming, A.J., Moheimani, S.R.: A broadband controller for shunt piezoelectric damping of structural vibration. Smart Mater. Struct. **12**, 18–28 (2003)
20. Park, C., Park, H.: Multiple-mode structural vibration control using negative capacitive shunt damping. J. Mech. Sci. Technol. **17**, 1650–1658 (2003)
21. Beck, B., Cunefare, K., Ruzzene, M., et al.: Experimental analysis of a cantilever beam with a shunted piezoelectric periodic array. J. Intell. Mater. Syst. Struct. **22**, 1177–1187 (2011)
22. Park, C.H., Baz, A.: Vibration control of beams with negative capacitive shunting of interdigital electrode piezoceramics. J. Vib. Control **11**, 331–346 (2005)
23. Date, M., Kutani, M., Sakai, S.: Electrically controlled elasticity utilizing piezoelectric coupling. J. Appl. Phys. 87, 863 (2000)
24. Imoto, K., Nishiura, M., Yamamoto, K., et al.: Elasticity control of piezoelectric lead zirconate titanate (PZT) materials using negative-capacitance circuits. Jpn. J. Appl. Phys. **44**, 7019–7023 (2005)
25. Chen, S.B., Wen, J.H., Yu, D.L., et al.: Band gap control of phononic beam with negative capacitance piezoelectric shunt. Chin. Phys. B **20**, 014301 (2011)
26. Chen, S.B., Wen, J.H., Wang, G., et al.: Tunable band gaps in acoustic metamaterials with periodic arrays of resonant shunted piezos. Chin. Phys. B **22**, 074301 (2013)
27. Chen, S.B., Wang, G., Wen, J.H., et al.: Wave propagation and attenuation in plates with periodic arrays of shunted piezo-patches. J. Sound Vib. **332**, 1520–1532 (2013)
28. Casadei, F., Delpero, T., Bergamini, A., et al.: Piezoelectric resonator arrays for tunable acoustic waveguides and metamaterials. J. Appl. Phys. **112**, 064902 (2012)
29. Airoldi, L., Ruzzene, M.: Design of tunable acoustic metamaterials through periodic arrays of resonant shunted piezos. New J. Phys. **13**, 113010 (2011)
30. Ginder, J.M., Nichols, M.E., Elie, L.D., et al.: Magnetorheological elastomers: properties and applications. Proc. SPIE **3675**, 131–138 (1999)

31. Li, W.H., Zhang, X.Z.: A study of the magnetorheological effect of bimodal particle based magnetorheological elastomers. Smart Mater. Struct. **19**, 035002 (2010)
32. Xu, Z.B., Gong, X.L., Liao, G.J., et al.: An active damping-compensated magnetorheological elastomer adaptive tuned vibration absorber. J. Intell. Mater. Syst. Struct. **21**, 1039–1047 (2010)
33. Liao, G.J., Gong, X.L., Xuan, S.H., et al.: Development of a real-time tunable stiffness and damping vibration isolator based on magnetorheological elastomer. J. Intell. Mater. Syst. Struct. **23**, 25–33 (2012)
34. Liao, G.J., Gong, X.L., Xuan, S.H.: Phase based stiffness tuning algorithm for a magnetorheological elastomer dynamic vibration absorber. Smart Mater. Struct. **23**, 015016 (2014)
35. Xu, Z., Wu, F.: Elastic band gaps of magnetorheological elastomer vibration isolators. J. Intell. Mater. Syst. Struct. **10**, 14535014 (2014)
36. Tang, H., Luo, C., Zhao, X.: Tunable characteristics of a flexible thin electrorheological layer for low frequency acoustic waves. J. Phys. D: Appl. Phys. **37**, 2331–2336 (2004)
37. Yeh, J.Y.: Control analysis of the tunable phononic crystal with electrorheological material. Phys. B: Condens. Matter **400**, 137–144 (2007)
38. Zhou, X.L., Chen, C.Q.: Tuning the locally resonant phononic band structures of two-dimensional periodic electroactive composites. Phys. B: Condens. Matter. **431**, 23–31 (2013)
39. Chen, Y.Y., Huang, G.L., Sun, C.T.: Band gap control in an active elastic metamaterial with negative capacitance piezoelectric shunting. J. Vib. Acoust. **136**, 061008 (2014)
40. Guo, N., Cawley, P.: The interaction of Lamb waves with delaminations in composite laminates. J. Acoust. Soc. Am. **94**, 2240–2246 (1993)
41. Lemistre, M., Balageas, D.: Structural health monitoring system based on diffracted Lamb wave analysis by multiresolution processing. Smart Mater. Struct. **10**, 504–511 (2001)
42. Liu, B., Shaw, M.T.: Electrorheology of filled silicone elastomers. J. Rheol. **45**, 641–657 (2001)
43. Hu, J., Chang, Z., Hu, G.K.: Approximate method for controlling solid elastic waves by transformation media. Phys. Rev. B **84**, 201101(R) (2011)
44. Chang, Z., Hu, J., Hu, G.K., et al.: Controlling elastic waves with isotropic materials. Appl. Phys. Lett. **98**, 121904 (2011)
45. Wu, T.T., Chen, Y.T., Sun, J.H., et al.: Focusing of the lowest antisymmetric Lamb wave in a gradient-index phononic crystal plate. Appl. Phys. Lett. **98**, 171911 (2011)
46. Schiller, N.H., Lin, S.C.S., Cabell, R.H., et al.: Design of a variable thickness plate to focus bending waves. In: ASME 2012 Noise Control and Acoustics Division Conference, New York City, New York, USA (2012)